OPTIMIZATION AND VERIFICATION OF A BRUSHLESS DC-MOTOR FOR CRYOGENIC MECHANISMS

M. Eggens[1], D. van Loon[1], H.P. Smit[1], W. Jellema[1], P. Dieleman[1], A. Detrain[1], M. Stokroos[1], A.C.T. Nieuwenhuizen[1]

[1]SRON Netherlands Institute for Space Research, Sorbonnelaan 2, 3584 CA Utrecht, The Netherlands
Email: M.Eggens@sron.nl

ABSTRACT

In this paper we report on the results of the investigation on the feasibility of a cryogenic motor for a Filter Wheel Mechanism (FWM) for the instrument SpicA FAR-infrared Instrument (SAFARI). The maximum allowed dissipation of 1 mW is a key requirement, as a result of the limited cooling resources of the satellite. Therefore a quasi 3D electromagnetic (EM) model of a Brushless DC (BLDC) motor has been developed. To withstand the severe launch loads a mechanical concept has been designed to limit the friction torque in the bearings. The model was verified by room temperature and cryogenic measurements on an existing motor from the test setup. The model shows that the proposed BLDC motor design fulfils the requirements.

1. INTRODUCTION

A consortium led by SRON Netherlands Institute for Space Research is developing the space instrument SpicA FAR-infrared Instrument (SAFARI). SAFARI is an imaging spectrometer for the 34 – 210 μm wavelength region scheduled for launch in 2022 on board the Space Infrared telescope for Cosmology and Astrophysics (SPICA), developed by leading agency JAXA. The SPICA mission will have a mechanically cooled mirror, providing sky background limited observations. The same mechanical coolers will also provide the SAFARI instrument with a 4.8 K interface temperature. The cooling power on board limits the allowed dissipation in the mechanisms to the mW range [1]. SAFARI will contain four mechanisms and only the Fourier Transform Spectrometer Mechanism is always operational. The other three mechanisms, two Filter Wheel Mechanisms (FWM) and a shutter mechanism will not be operated simultaneously and therefore the remaining dissipation budget can be shared. Apart from the constraint given by the cooling capacity the detectors of SAFARI require a maximum temperature of any element to be below 12 K.
In chapter 2 we describe a conceptual mechanical design of a FWM to estimate the expected friction torque of the bearings and Moments of Inertia (MoI) of the rotor part. A quasi 3D EM model will be presented in chapter 3, including the verification of the model by measurements on an existing BLDC motor. Chapter 4 describes the steps to come to an optimum design of the motor. Chapter 5 lists possible alternative approaches. Conclusions are drawn in chapter 6.

2. DESCRIPTION FWM

2.1. Key requirements FWM

The allowed heat flow of the FWM is 1 mW on the thermal strap between the instrument and the spacecraft cooler. The time to move the mechanism π radians is 60 seconds with the total Joule losses constrained to 60 mJ. This thermal budget should include all losses, such as mechanical friction, eddy current and Joule losses in the motor, position sensors and harness. Because the maximum allowed instantaneous heat flow is limited, the dynamics of the thermal interface should be accounted for as well. The thermal interface is modelled as a first order low pass filter with a time constant determined by the heat capacity of 7.6 J/K (20 kg of aluminium at 4.8 K) and a strap heat resistance of 0.1 W/K leading to a time constant of approximately 76 seconds [1].
The dimensions for the FWM are limited due to the compact optical design and envelope of the SAFARI instrument. This leads to a maximum filter wheel diameter of 200 mm and a thickness of 25 mm. The volume of the bearing system plus motor is set to a size of 100 mm (square) and a thickness of 75 mm. The total mass of the FWM should be smaller than 1.2 kg and should be able to survive launch loads of 16 g_{rms}.

2.2. Conceptual design FWM

A conceptual mechanical design is contrived to estimate the MoI of the rotor and friction torque of the bearings that result in mechanical and electrical losses. The FWM consists of three main components: the wheel, the motor and the bearing system. The basis is a direct drive configuration, which means that the three main components are assembled on the same axis. In this approach complex and dissipative transmissions, e.g. gearings, are avoided. Fig. 1 shows a cross section of the three main components in the FWM.
The filter wheel consists of 6 filter positions with a clear aperture of 35 mm each. Aluminium 6061-T6 is used as basis for the mechanical structure.
The C84 motor from the Low Temperature Laboratory (TTL) from the Free University of Berlin [2] is used as

representative for volume, mass and MoI. The C84 motor has an outer diameter of 84 mm and a thickness of 22 mm.

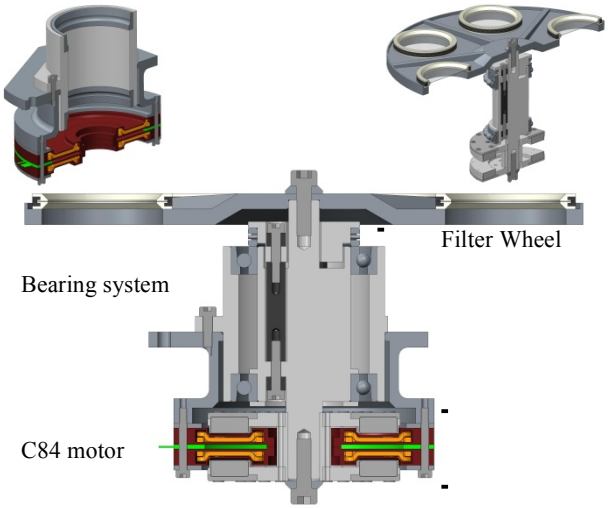

Figure 1. Cross section of FWM conceptual design. Top left shows the stator part and top right the rotor part.

The bearing system is an assembly of various components that connect the rotor and stator by two angular contact ball bearings. Fig. 2 shows a cross section of the bearing system.
Because of differences in Coefficient of Thermal Expansion (CTE) we chose to create relevant parts of the same material. This avoids extra forces on the bearings that lead to a higher friction torque at 4.8 K. Stainless steel, e.g. AISI 440C, is used for the bearing housing, the axes and the bearings. This approach was successfully applied to the mechanisms of the MIRI [3] and NIRSPEC [4] instruments.
Besides the mounted bearings, the bearing housing contains also the mechanical interface with the SAFARI instrument. The Centre of Gravity (CoG) of the rotor is between both bearings and at the axis of revolution to create a balanced system. Nevertheless a locking device is needed to lock the wheel in each filter position.
Friction torque creates mechanical losses. Referring to [3] we estimated a friction torque of 10 mNm (including margin) due to the bearings. The energy needed to rotate the wheel π radians is simply π times the friction torque. Therefore a friction torque of 10 mNm takes half of the 60 mJ full energy budget for the entire FWM. The remaining energy budget or 0.5 mW dissipation is set to the other dissipative components of the FWM.
However, through the torque constant, the friction torque also drives the current in the motor and harness and therefore the electrical Joule losses. Reducing the friction torque is therefore the most essential step in developing a low power cryogenic actuator.
Mounting the bearings with a well defined pre-load and lubrication like MoS_2 reduces the friction torque. For the conceptual design of the FWM we chose to apply a pre-load of 120 N, which is based on experiences with the MIRI mechanism [3]. A certain pre-load is necessary to overcome sliding effects inside the bearing. However this pre-load is not sufficient to survive the high launch loads of 16 g_{rms}. To avoid hammering of the bearings a minimum pre-load of 300 N is needed to carry a mass of the rotor of 0.6 kg.
Because the launch is under warm conditions the cool down of the FWM is used to reduce the pre-load. Therefore the bearings are foreseen with a customized stainless steel spring, which applies a force of 300 N with a deflection of 150 µm at 300 K. The desired low pre-load of 120 N at 4 K will be achieved when the deflection decreases with 90 µm using the difference in CTE of 0.3 % between stainless steel housing and three invar rods. The main advantage of this approach is a well controlled and defined pre-load that leads to a reproducible result for the friction torque.

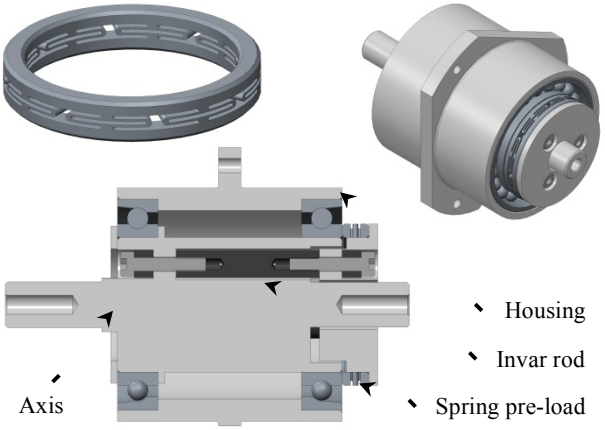

Figure 2. Cross section of the bearing system (bottom). Top left shows a conceptual spring to apply a defined pre-load. Top right shows the whole assembly.

2.3. Results FWM

The conceptual design fits within the constrained volume and includes a feasible adjustable spring to control the pre-load and as a result also the friction torque. The 3D-model predicts a MoI of the rotor of $1.66 \cdot 10^{-3}\,\mathrm{kg \cdot m^2}$ and a mass of 1.5 kg. Further work has to done to implement a locking device, light tight interfaces and optimizing mass and effects of lubrication. The friction torque due to the bearings is set to 10 mNm, which results in an average dissipation of 0.5 mW or an energy of 30 mJ for π radians movement.

3. DESCRIPTION MOTOR FWM

3.1. Key requirements motor FWM

As a result of the conceptual design of the FWM the maximum outer dimensions of the motor is set to a diameter of 80 mm and a thickness of 20 mm. Within this volume the motor should contain redundant coils

that need to be used in case the primary coils fail unexpectedly. Other aspects like the amount and shape of the permanent magnets and coils, length air gap and other internal dimensions may be filled as desired.
The total thermal budget of 1 mW is divided into mechanical losses and dissipation in the electrical harness, coil windings, position sensors and locking device. To overcome the total estimated 10 mNm friction torque as explained in chapter 2.2 an initial thermal budget was set to the FWM motor. This budget applies to the electrical Joule losses in the coil windings and its electrical harness and was estimated to be 0.3 mW for 60 seconds. With these numbers the motor requires a motor constant of 0.6 Nm/√W at 4.8 K.

3.2. Concept motor FWM

Modelling of the selected motor has been started in order to verify whether if the interface requirements can be met. The selected motor is an air cored axial flux permanent magnet Brushless DC (BLDC) type, with a high efficiency, low dissipation and simple reliable mechanical and electrical design. TTL used similar motors under cryogenic conditions in earlier flight instruments [2] and BLDC motors therefore is known for its cryogenic properties and space heritage. Current motor constant of type C84 is 0.3 Nm/√W at 4.2 K, which is half of the required motor constant to drive the FWM. Experience showed that we had to choose for a 2-phase motor. The model of the BLDC-motor is based on an operation principle that is represented in Fig. 3.

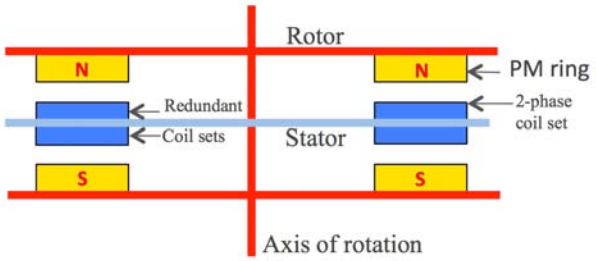

Figure 3. Cross section of an air cored axial flux permanent magnet motor with redundant coil sets.

There are two basic rules. Two permanent magnets at each side of the stator will have opposite polarity as well as two adjacent permanent magnets on one rotor Permanent Magnet (PM) ring. This will create a flux in the axial direction. The rotor consists of two parts each holding a set of magnets. At the outer side, the rotor also needs to contain a piece of high permeability material (back-iron) to close the flux path between magnets. Note that in this paper only circular permanent magnets are assumed, although this is not a model limitation. Fig. 4 shows the motor conceptually from above assuming that there are twelve circular permanent magnets and thus six poles. The permanent magnets are placed on a ring constrained by the inner and outer diameters R_{in} and R_{out}. A circle with average radius will cross the centre of the permanent magnets and is defined as R_{av}. The blue and green lines show the approximate shape of the trapezoidal coils for a 2-phase motor and therefore the two phases have a mechanical phase shift equal to a half permanent magnet diameter D_{pm}, creating a 90 degrees electrical offset between the two phases.

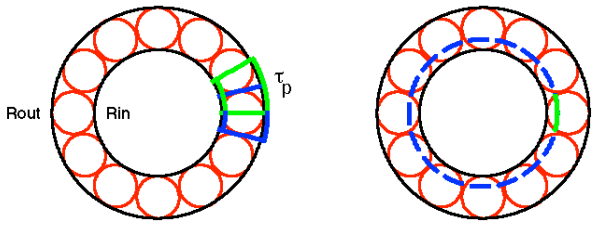

Figure 4. Left) View in axial direction of an axial flux permanent magnet machine. Right) Radial slice intersection with the permanent magnet.

3.3. Quasi 3D motor model

The purpose of the computational model is to verify conceptual motor designs within 15% of accuracy such that different motor geometries can be analysed over different parameter ranges within a small amount of time. Therefore solving a full 3D model with the Finite Element Method (FEM) of the motor was abandoned, as this would not allow fast computation of different geometries. Instead a quasi 3D model has been developed for the computation of the magnetic field based on existing literature [5].
The quasi 3D approach will subdivide the radius distance between R_{out} and R_{in} into N_{slice} sections called radial slices. For each radial slice a 2D magnetic field due to the permanent magnets is computed. First the intersections of the radial slice (blue line right Fig. 4) with the permanent magnets are computed. This allows the magnets to have any shape. For an ideal motor, it is enough to compute the intersections for two magnets only, as the result will be just a repetition over the circumference. However, when FEM is used more accurate results are obtained with four magnets to avoid the effect of field fringing at the boundary. Last step is "unfolding" the radial slice to allow the analysis in a 2D model.

3.4. Results quasi 3D motor model

The first analysis has been performed in an open source finite element tool (FEMM v4.2) and the result is shown in Fig. 5. In the middle of the air gap the flux density (ideally) is varying sinusoidal with respect to the angular position of the rotor (sinusoidal curve in Fig. 5). The red and blue dots show the coil wire bundles on the stator with direction out of and into the 2D plane respectively for each phase. Here the coil width is assumed to be equal to D_{pm} or “full-pitched”.

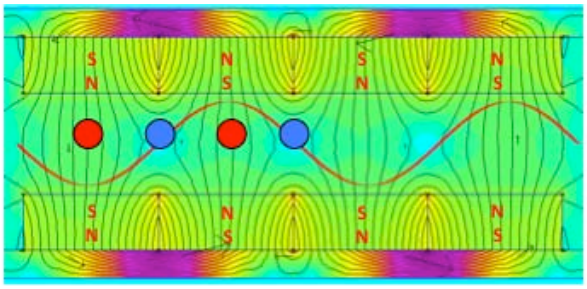

Figure 5. Example of an unfolded circular slice at R_{av} with four permanent magnets used in a FEM analysis.

In this representation a current in the left red wire will experience a maximum negative flux density whereas the other red wire will experience a positive flux density with an opposite current direction. As the Lorentz force scales with the flux density times the current in the wire, the total Lorentz force in this situation is twice the force for a single wire bundle. Note that in this example the Lorentz force acting on the blue wires is zero. Fig. 6 shows an example of a 2D computation for a radial slice closer to R_{in}, which leads to a smaller cross-section of the radial circle with the permanent magnet.

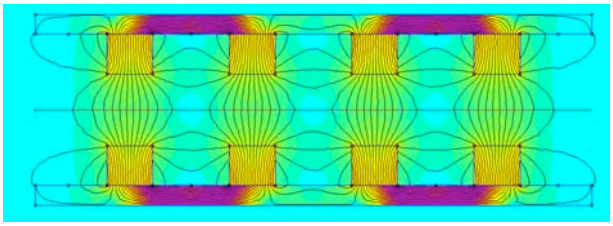

Figure 6. Example of small cross section of circular slice starting from R_{in} and permanent magnets.

The sinusoidal flux density is not ideally over the entire air gap height, but is more of a block wave once the flux density is computed near the surface of the permanent magnets. Therefore the flux density in the axial direction needs to be computed as well. Although Matlab can control the FEM application the analysis still takes a lot of computation time. Instead, the magnetic flux density is computed by using analytical equations based on a Fourier component analysis as is performed in [6]. Variations in the air gap in axial direction are also taken into account by using the extension derived in [7].

The model is written in Matlab and the flux density is computed directly over the circumference for each axial height and slice number. Fig. 7 shows good agreement between the computed flux density in the centre of the air gap with FEM (Blue) and Analytical (Red).

In principle the flux density due to a current in the coils can change the magnetic field as well, which is called armature reaction. As in the target application the currents are considered low (< 20 mA), the effect will be smaller than 0.2% from simulation results.

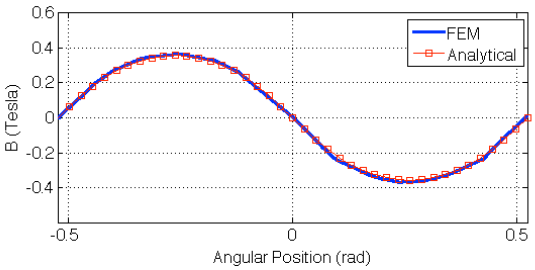

Figure 7. Flux density computed in unfolded (2D) circular slice at R_{av} in middle of the air gap with FEM analysis and directly based on analytical equations.

Putting all items together, the model consists of motor geometry definition followed by the computation of the flux density along the circumference for each radial slice. The axial part is taken into account by dividing the coil height in N_y parts and by repeating the field procedure for each axial component.

Now the torque produced by the motor needs to be determined. This can be accomplished in two different ways. By using the Lorentz force or the flux linkage method. Both methods are included in the model for verification purposes, however the flux linkage is easier to use and is used as the default method.

A similar procedure is followed as in the computation of the flux density in the air gap. Only in this step the intersections of the radial slice (blue right Fig. 4) with the coil geometries (blue and green lines left Fig. 4) are computed. For trapezoidal shaped coils this step is not strictly necessary as angle relationships can be directly used. Next, the flux linkage λ per coil is computed according to Eq. 1 where N_{slice} and N_{turns} are the number of slices and number of turns at the same gap height respectively, B is the flux density due to the permanent magnets and ds is the area between the two wires that enclose the flux.

$$\lambda(\theta) = \sum_{n=1}^{N_{slice}} \sum_{k=1}^{N_{turns}} \oiint B_{nk}(\theta) ds_{nk} \tag{1}$$

When more wires are stacked together (N_{stack} >1) the flux density over the coil height (N_y terms) is averaged first. Eq. 1 is used and the result is multiplied with N_{stack}. This entire process is repeated for several angular displacements θ of the stator and hence coils versus the static magnetic flux density. The total angular displacement is equal to an electrical period or $(2\pi)/(N_{pm}/2)$ where N_{pm} is the number of magnets per rotor and $N_{pm}/2$ is the number of poles.

Now the derivative of the flux linkage versus time gives the back EMF voltage. Normally this EMF value is specified for 1 rpm rotation and thus by scaling the previous flux linkage computation over one electrical period such that the angular speed equals $2\pi/60$ rad/s, the EMF voltage per 1 rpm is found. The maximum

total torque produced by an ideal 2-phase motor is constant and is exactly equal to the maximum of the EMF waveform times the peak current in the phases, divided by the angular velocity, which in our definition is $2\pi/60$ rad/s. The result is equal to the torque constant.

3.5. Quasi 3D model verification

The C84 motor has been acquired based on the design in [2]. This 2-phase motor has 12 Sm_2Co_{17} circular permanent magnets and 12 full pitched coils per phase, each having 230 turns. The windings are redundant and placed symmetrically with respect to the stator. D_{pm} is 12 mm. The specified torque constant for the C84 motor is 0.4 Nm/A per phase or 0.8 Nm/A when the redundant windings are connected in series.
An important step in verifying the quasi 3D model is the measurement of the magnetic flux density in the air gap. The measurement has been performed at room temperature with a 3D Hall sensor from Aeropoc that is mounted on a translation table as is shown in Fig. 8.

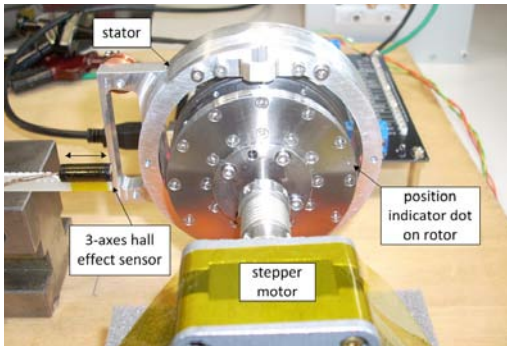

Figure 8. Flux density measurement setup C84 motor (TTL). An external stepper motor drives the C84 axis.

The inner stator in the C84 motor is removed to give the sensor access to the air gap. The motor can be positioned to various angles with a stepper motor that is connected to the axis. By repeating the measurements with the Hall sensor for different radii the flux density can be measured. The result is compared to simulation results, which are presented in Fig. 9.
The shape of the curves shows good similarity. Only at the outer boundary they show a discrepancy. This is due to the quasi 3D method that can only compute a field where a piece of magnet is still present and therefore fields outside D_{out} will be zero by default which cannot be realized in practice. The error due to this effect is considered to be negligible, although this should be assessed in more detail.
The geometry of the motor was put in the model and the EMF waveform has been computed from which the torque constant had been determined. Some parameters are uncertain, such as the specification of the magnets.
The model uses a remnant flux density of 1.07 T, a relative permeability of 1.1 leading to an energy density of 27 MGOe. With these numbers, the simulated EMF peak voltage at 1 rpm is 55 mV_p leading to the a total torque of 0.52 Nm/A_p. The torque constant per phase gives a $\sqrt{2}$ scaling or 0.37 Nm/A. This is 8 % off on the specification of the torque constant of the C84 motor.

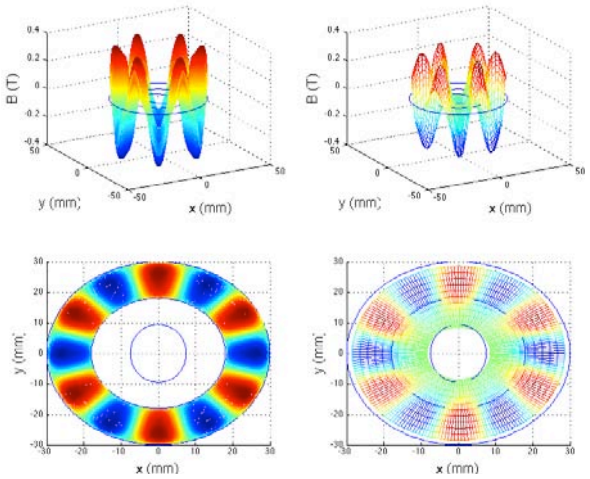

Figure 9. Flux density simulation (l) and measurements (r) in the middle of the air gap of C84 motor.

The back EMF waveforms have been measured for the C84 motor by driving the axis at constant speed. In this case the normal and redundant coil sets were connected in series to double the output voltage. The measurements and simulated results for 4 rpm are shown in Fig. 10 (red and blue line respectively). Because of the good agreement between measurement and simulation results, the model is assumed to be sufficient for optimization purposes.

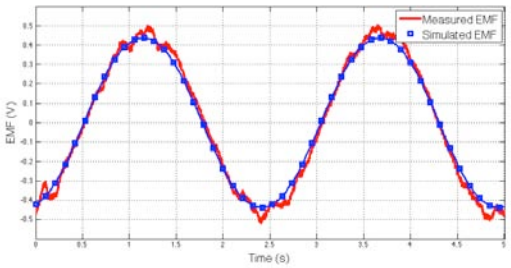

Figure 10. Measured EMF waveform on one phase C84 motor (series nominal and redundant) (red), and simulated EMF from model at 4 rpm (blue).

4. OPTIMIZATION AND RESULTS FWM

4.1. Control and dynamic simulation

As the back EMF is ideally sinusoidal the applied currents to the coils are also sinusoidal and in phase with the EMF signals, leading to a constant output torque. The motor has two Hall sensors to measure the magnetic field in the air gap. Both are positioned such that there exist a 90-degree phase difference in the experienced magnetic flux density. These sensors will

produce sine and cosine output signals with constant frequency when the motor is running at constant motor speed. Next the controller uses these signals as a sin/cos encoder input and computes the angle between these two signals. From this result the position within an electrical period (a pole) can be determined. Finally the control output, that represents the amplitude of the sinusoidal phase currents, is remapped again to the sin/cos reference frame.

For the power estimation a less complicated model is created consisting of a simple state space description of the motor with voltage control, with ignoring of the sin/cos control plane. Instead the controller uses position as input and current, representing the amplitude of the sinusoidal phase currents, as output. The controller is also implemented in Matlab and uses the derived torque constant from the quasi 3D model along with a measured or estimated moment of inertia of the motor and load, coil inductance and coil and harness resistance. The controller is of the full state feedback type such that all poles can be placed and two dominant highly damped complex conjugate poles determine the dynamics. This allows the assessment of dominant pole location and hence settling time on the power dissipation.

As already mentioned, friction is the main driver for dissipation and should be included. As dry lubrication is assumed, the viscous damping term is estimated to be low (1.2 mN s/m) Therefore the dominant term is Coulomb friction. This friction is constant with angular velocity and depends only on the sign of this type of velocity. Moreover it should be zero when the velocity is zero. However, this transition would be impossible to simulate with an Ordinary Differential Equation (ODE) solver as the function is non-differentiable. Instead a transition region is defined and the Coulomb friction is modelled as a tanh function, which gives a certain transition region and is still differentiable. To obtain stable simulation results static friction is finally added in this simple model by evaluating, within the transition region, if the applied electromagnetic torque is smaller than the Coulomb friction. If so, then the Coulomb friction torque is set equal to the electromagnetic torque. Note that the Dahl friction model does not include this effect and leads to instability as well. The more sophisticated Lugre friction model has not – yet – been evaluated.

For power evaluation a step input of π radians is set to the control loop reference input. Because in the state space model all relevant variables are present (currents, resistances, angular speed, friction torque) all dissipation terms in the motor can be computed. Although the speed is low, eddy current losses in the coil windings are computed as well. At this moment constant dissipation terms, such as Joule losses in the Hall sensors, are only considered during the settle time based on the assumption that these components can be turned off when the motor has reached its position. This requires some kind of hold actuator, but this is not within the scope of this paper. The settle time is estimated as $-4/\mathrm{real}(p_{1,2}) \times \log(50)$, with $p_{1,2}$ equal to the two dominant poles. Simulations for different dominant pole locations show that an optimum pole placement exists that minimizes the dissipation in the motor. This is caused by two contradicting terms. A low settling time reduces the Joule losses due to overcoming the friction torque and associated electrical Joule losses, Hall sensor dissipation etc. whereas this increases the Joule losses during the acceleration of the wheel, viscous damping loss and eddy current loss.

4.2. Coil windings motor

There are multiple winding schemes for permanent magnet motors. The implementation used in [2] is the winding scheme shown in Fig. 11. The windings of both phases are at the same air gap height and need to be folded for that reason. This manual work is very delicate and difficult especially when the number of coil windings need to be increased to reduce dissipation. Moreover the part of the windings that do not contribute to torque production, the end windings, are relatively large as the coils need space to accommodate the folding, reducing the efficiency of the motor.

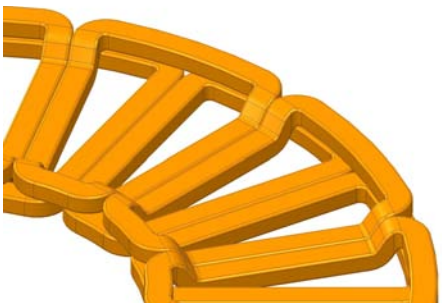

Figure 11. Example of folded windings for a 2-phase full pitched coil motor.

Alternatively the coil sets can be split in two separate sets within the air gap making assembly and manufacturing of flat trapezoidal coils much easier. As redundancy requirements alone ask for two 2-phase coil sets, this means that four single coil sets are needed. The stacking of coil sets has a significant impact on the air gap height and therefore reduces the peak magnetic flux density, which makes the motor less efficient. Despite of this effect we chose to stack the coils to increase the number of windings, which easily can be manufactured by using orthocyclic-winding coils.

4.3. Position sensor motor

In the C84 two KSY10 Hall sensors have been used to measure the angular position. However, these components are obsolete. An alternative was found after

measuring several Hall sensors at 4 K in the motor application. From these tests it showed that the optimal sensor is the HE-144 from Hoeben. As power dissipation is important, the bias current has been varied as well. A bias current of 0.5 mA gave a voltage of 0.3 V (40% lower than at room temperature) and a voltage output of 60 mV_{pp} with sufficient dynamic range. The dissipation of the sensor used in the model is equal to 0.15 mW. Note that space qualification of the component might still be an issue.

4.4. Optimization and final results

The FWM concept use NdFeB permanent magnets (N42 type) instead of Sm_2Co_{17} to increase the remnant flux density from 1.07 T to 1.27 T. SRON has used these type of magnets in the chopper and the diplexer mechanism of the HIFI instrument and have been tested down to 4 K successfully [8].
The other change for the C84 motor was an optimized number of wiring, leading to 30 windings x 10 windings stacked, or 300 turns per coil for 12 coils per phase. The winding core diameter is 100 µm with 10 µm insulation thickness. Total number of turns per phase is then 3600 and will fit in the available volume for the motor.
The derived total torque constant is 0.9 Nm/A_p with a resistance of 3.9 Ohm per phase at 4 K. Fig. 12 shows the computation of the motor constant versus number of coil windings in a plane and versus the windings stacked in axial direction.

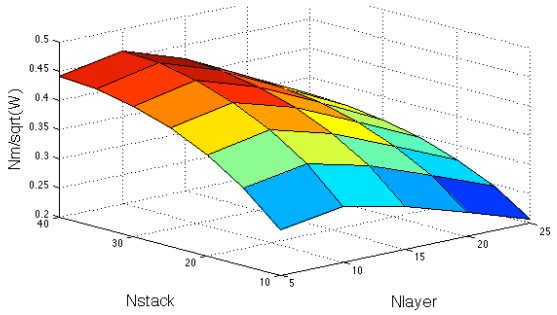

Figure 12. Computation of Motor Constant motor only versus number of wires in a plane and wires stacked.

Stacking wires will increase the air gap and will reduce the flux density. At the same time increasing the windings in a plane will average the flux density seen by the coil wire, which will reduce the torque production as well. Although a higher number of windings do increase the motor constant when a high resistive harness is used, this number still is a good compromise. The quasi 3D model for the FWM concept has been simulated and the dynamic model was run. The results of this dynamic power estimation with manually optimized complex poles (-1±0.1i rad/s) are shown for the 2-phase concept in Fig. 13. The top of the figure shows the angle (black) and velocity (red). The middle curve shows the Coulomb friction experienced (black) and current needed (red). The bottom figure then shows the computed power contributions.

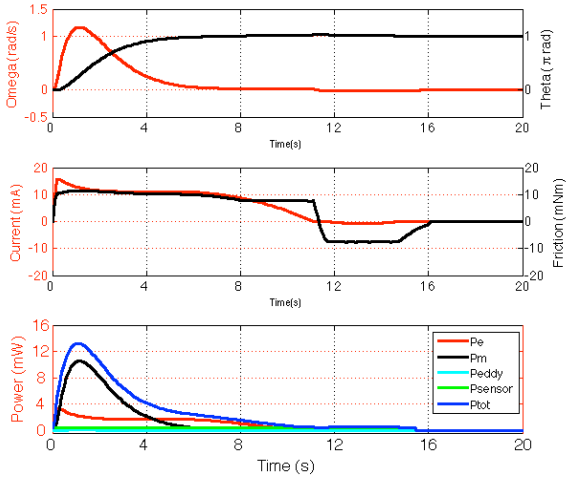

Figure 13. Dynamic simulation for a 180 degrees step input and associated power dissipation 2-phase motor.

Note that within the power dissipation, a harness resistance of 6.7 Ohm is used per wire (13.4 Ohm per phase in the 2-phase motor), which is equal to the harness resistance between 30 K and 4.8 K.
As described earlier the dissipation on the thermal strap is more important and can be easily determined by filtering the total dissipation with a time constant of 76 s as described earlier. The final result for optimized 2-phase motor is given in Fig. 14. The maximum heat flow on the thermal strap is about 0.7 mW and is clearly below the specified 1 mW.

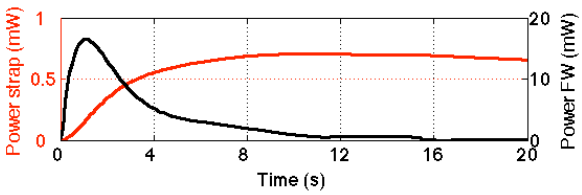

Figure 14. Total dissipation for 180 degree step (black) and dissipation at power strap (red) 2-phase motor.

5. ALTERNATIVE DESIGN FWM

Another conceptual FWM design has been created based on an integrated mechatronic system approach.
Using 3-phases makes it possible to do this efficiently by changing the coil width equal to $2/3D_{pm}$. In this setup the number of coils per phase is reduced (divided by 3) and therefore more windings per coil will be needed for the same torque constant. Instead in this conceptual design the torque production is increased by integrating the motor in the wheel itself, making full use of the increase in arm length. Increasing the circumference while keeping the magnets and hence coils similar in size, increases the number of coils again, reducing the

number of turns per coil. Due to the large harness resistance of 6.7 Ohm, the coil resistance has much less impact on the overall dissipation. This makes it even possible to use PCB type of windings. A disadvantage is the permanent magnet mass and MoI increase and care was taken to minimize this value. A compromise was found with a D_{pm} of 8 mm for a total of 120 magnets, doubling the mass from 110 g to 240 g. MoI is increased to $5.7 \cdot 10^{-3}\,\mathrm{kg \cdot m^2}$. The 3-phase motor requires at least 3 Hall sensors. The integrated concept gives a more compact result as can be seen in Fig. 15.

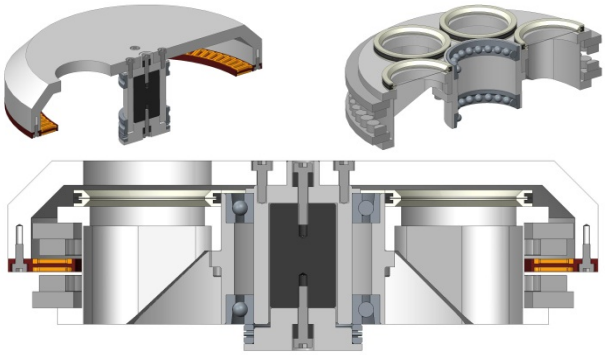

Figure 15. Alternative design FWM with a 3-phase integrated border motor. Top left shows the stator part and top right shows the rotor part.

For the alterative 3-phase motor concept, 96 turns per coil were used for in total 30 coils per phase. This resulted in a torque constant of 1.1 $\mathrm{Nm/A_p}$ with a phase resistance of 6.6 Ohm. The total dissipation with a time constant of 76 s is shown in Fig. 16. The maximum heat flow on the thermal strap is about 0.6 mW.

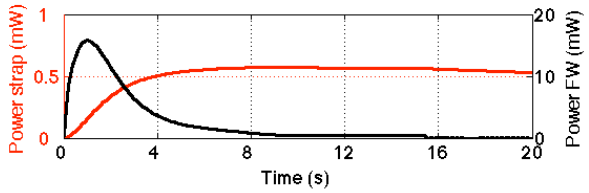

Figure 16. Total dissipation for 180 degree step (black) and dissipation at power strap (red) 3-phase motor.

6. CONCLUSIONS

The BLDC quasi 3D EM model corresponds with the measurement on the existing motor very well. Together with a control and dynamic simulation the 3D model shows that the conceptual FWM including an optimized 2-phase motor meets the requirement for peak dissipation of 1 mW. There is sufficient margin included to accommodate uncertainties and a locking device if needed.

7. ACKNOWLEDGEMENT

The authors would like to thank Dr. A. Poglitsch and Dr. J. Schubert from the Max-Planck-Institute für Extraterrestrische Physik (MPE) for their support and verification of the quasi 3D-model. The authors also acknowledge the discussions with Ir. E. Renotte from the Centre Spatial de Liège (CSL) concerning the PACS mechanism. Finally, the authors also acknowledge Mrs. M. Schoele and Mr. U. Ruppert from TTL (Free University of Berlin) for their support and delivery of the C84 motor.

8. REFERENCES

1. Charles, I., et al. (2012). Thermal architecture of the SPICA/SAFARI Instrument. *Millimeter, Submillimeter, and Far-Infrared Detectors and Instrumentation for Astronomy VI. Proc. of the SPIE, Volume 8452.*

2. Arend, I., et al. (2011). Cryogenic motors for Herschel/PACS and JAMES WEBB/MIRI and NIRSPEC. *European Space Mechanisms and Tribology Symposium, Constance.*

3. Kraus, O., et al. (2008). Cryogenic wheel mechanisms for the Mid-Infrared Instrument (MIRI) of the James Webb Space Telescope (JWST): detailed design and test results from the qualification program*, proc. of SPIE volume 7018.*

4. Neugebauer, C., et al. (2009). NIRSPEC wheel support mechanisms central duplex bearings cryogenic test results. *European Space Mechanisms and Tribology Symposium, Vienna.*

5. Parviainen, A., Niemelä, M. and Pyrhönen, J. (2004). Modeling of axial flux permanent-magnet machines. *IEEE Trans. Ind. Appl., vol. 40, no. 5, pp. 1333–1340.*

6. Bumby, J.R. and Martin, R. (2005). Axial-flux permanent-magnet air-cored generator for small-scale wind turbines. *IEE Proc.-Electr. Power Appl., Vol. 152, No. 5, pp 1065-1075.*

7. Price, G.F., Batzel, T.D., Comanescu, M., Muller, B.A. (2008). Design and Testing of a Permanent Magnet Axial Flux Wind Power Generator. *Proceedings of the 2008 IAJC-IJME International Conference ISBN 978-1-60643-379-9, Paper 190, ENT 202.*

8. Huisman, R., et al. (2011). Cryogenic mechatronic design of the HIFI Focal Plane Chopper, *Mechatronics, doi:10.1016/j.mechatronics.2011.03.004*